Monthly Notices of the ROYAL ASTRONOMICAL SOCIETY

MNRAS **523,** 3239–3250 (2023) https://doi.org/10.1093/mnras/stad1385
Advance Access publication 2023 May 08

H_2CN/H_2NC abundance ratio: a new potential temperature tracer for the interstellar medium

D. San Andrés [1]★ L. Colzi [1] V. M. Rivilla [1] J. García de la Concepción,[2,3] M. Melosso,[4] J. Martín-Pintado,[1] I. Jiménez-Serra,[1] S. Zeng [5] S. Martín[6,7] and M. A. Requena-Torres[8,9]

[1]*Centro de Astrobiología (CAB), INTA-CSIC, Carretera de Ajalvir km 4, Torrejón de Ardoz, 28850, Madrid, Spain*
[2]*Departamento de Química Orgánica e Inorgánica, Facultad de Ciencias, Universidad de Extremadura, E-06006 Badajoz, Spain*
[3]*IACYS-Unidad de Química Verde y Desarrollo Sostenible, Facultad de Ciencias, Universidad de Extremadura, E-06006 Badajoz, Spain*
[4]*Scuola Superiore Meridionale, Largo San Marcellino 10, I-80136 Naples, Italy*
[5]*Star and Planet Formation Laboratory, Cluster for Pioneering Research, RIKEN, 2–1 Hirosawa, Wako, Saitama 351–0198, Japan*
[6]*European Southern Observatory, Alonso de Córdova, 3107, Vitacura, Santiago 763–0355, Chile*
[7]*Joint ALMA Observatory, Alonso de Córdova, 3107, Vitacura, Santiago 763–0355, Chile*
[8]*Department of Astronomy, University of Maryland, College Park, MD 20742–2421, USA*
[9]*Department of Physics, Astronomy, and Geosciences, Towson University, Towson, MD 21252, USA*

Accepted 2023 May 4. Received 2023 May 4; in original form 2023 January 20

ABSTRACT

The H_2NC radical is the high-energy metastable isomer of H_2CN radical, which has been recently detected for the first time in the interstellar medium towards a handful of cold galactic sources, besides a warm galaxy in front of the PKS 1830−211 quasar. These detections have shown that the H_2CN/H_2NC isomeric ratio, likewise the HCN/HNC ratio, might increase with the kinetic temperature (T_{kin}), but the shortage of them in warm sources still prevents us from confirming this hypothesis and shedding light on their chemistry. In this work, we present the first detection of H_2CN and H_2NC towards a warm galactic source, the G+0.693−0.027 molecular cloud (with $T_{kin} > 70$ K), using IRAM 30-m telescope observations. We have detected multiple hyperfine components of the $N_{K_aK_c} = 1_{01}$–0_{00} and 2_{02}–1_{01} transitions. We derived molecular abundances with respect to H_2 of $(6.8 \pm 1.3) \times 10^{-11}$ for H_2CN and of $(3.1 \pm 0.7) \times 10^{-11}$ for H_2NC, and an H_2CN/H_2NC abundance ratio of 2.2 ± 0.5. These detections confirm that the H_2CN/H_2NC ratio is $\gtrsim$2 for sources with $T_{kin} > 70$ K, larger than the ∼1 ratios previously found in colder cores ($T_{kin} \sim 10$ K). This isomeric ratio dependence on temperature cannot be fully explained with the currently proposed gas-phase formation and destruction pathways. Grain surface reactions, including the $H_2NC \rightarrow H_2CN$ isomerization, deserve consideration to explain the higher isomeric ratios and H_2CN abundances observed in warm sources, where the molecules can be desorbed into the gas phase through thermal and/or shock-induced mechanisms.

Key words: astrochemistry – line: identification – ISM: clouds – ISM: molecules – Galaxy: centre.

1 INTRODUCTION

Since the first detection of CH in space by Swings & Rosenfeld (1937) and McKellar (1940), the rapid development of new instrumentation (especially at infrared and mainly at radio wavelengths) has led up to date to the confirmed detection of about 290 molecules[1] in the interstellar medium (ISM) or circumstellar shells within our own Galaxy (McGuire 2022). Recently, it has been reported the first detection in space of H_2NC (aminomethylidyne), the high-energy metastable isomer of the well-known H_2CN (methylene amidogen radical). Cabezas et al. (2021) and Agundez et al. (2023) have detected both isomers towards seven cold dense clouds, and also towards a $z = 0.89$ galaxy in front of PKS 1830−211 quasar (hereafter PKS 1830−211). They found that the H_2CN/H_2NC abundance ratio is ∼1 towards the cold clouds (with gas kinetic temperatures, T_{kin}, of ∼10 K), but higher (∼4) towards the warmer PKS 1830−211 ($T_{kin} \gtrsim 80$ K; Henkel et al. 2008). This suggests that the H_2CN/H_2NC ratio might be sensitive to the kinetic temperature, similar to the better studied HCN/HNC ratio (e.g. Irvine & Schloerb 1984; Schilke et al. 1992; Hacar, Bosman & van Dishoeck 2020). The HCN/HNC abundance ratio has been found to be ∼1 towards cold clouds ($T_{kin} < 20$ K; Sarrasin et al. 2010; Colzi et al. 2018), but $\gtrsim$1 in warmer sources (Liszt & Lucas 2001; Colzi et al. 2018). Hacar et al. (2020) explored the use of the HCN/HNC abundance ratio as a potential chemical thermometer in a large-scale map of the Orion molecular cloud, and found a linear dependence between the HCN/HNC ratio and the gas T_{kin}. They found the lowest ratios (∼1–4) towards the coldest regions ($T_{kin} < 30$ K), while the higher ratios (>5) were associated with the warmer sources ($T_{kin} \gtrsim 30$ K).

Agundez et al. (2023) searched for H_2CN and H_2NC towards two warm galactic diffuse clouds with $T_{kin} > 30$ K (Liszt, Lucas & Pety 2006; Liszt, Pety & Lucas 2010; Chantzos et al. 2020) unsuccessfully. The lack of detections of H_2NC and H_2CN towards warm galactic sources, besides the extragalactic ISM, prevents the

★ E-mail: dsanandres@cab.inta-csic.es
[1]https://cdms.astro.uni-koeln.de/classic/molecules.

confirmation to what extent the H_2CN/H_2NC ratio is indeed sensitive to the temperature. New detections of both isomers towards warm sources are required to gain insight about the chemistry of these molecular species.

We present the first detection of both H_2NC and H_2CN isomers towards a warm galactic molecular cloud: G+0.693−0.027 (hereafter G+0.693). This source, located within the Galactic Centre Sgr B2 complex, exhibits high T_{kin} (∼70–140 K; Zeng et al. 2018). G+0.693 is suggested to be affected by low-velocity shocks as a consequence of large-scale cloud–cloud collisions, responsible for the release into the gas phase of molecules formed on the dust grain surfaces (Martín et al. 2008; Zeng et al. 2020). This produces an extremely rich chemical reservoir; in fact, more than 120 molecular species have been already identified, including many nitrogen-bearing species (Requena-Torres et al. 2006, 2008; Rivilla et al. 2018, 2019, 2020, 2021a, b, 2022a, b, c; Zeng et al. 2018, 2021; Jiménez-Serra et al. 2020, 2022; Rodríguez-Almeida et al. 2021a, b; Colzi et al. 2022).

This article is organized as follows: in Section 2 we present the data of the observational survey towards G+0.693, while in Section 3 we describe the identification of H_2CN and H_2NC and analysis procedures we have followed as well as the summary of the main findings. In Section 4, we study the possible link between the H_2CN/H_2NC ratio and T_{kin}, and the potential use of this ratio as a thermometer. We also present a discussion on the interstellar chemistry of H_2CN and H_2NC, exploring their main formation and destruction routes. Finally, the conclusions are summarized in Section 5.

2 OBSERVATIONS

We have analysed data from a high-sensitivity spectral survey carried out towards G+0.693 (Rivilla et al. 2020, 2021a; Zeng et al. 2020). Single-dish observations centred at $\alpha_{J2000} = 17^h47^m22^s$ and $\delta_{J2000} = -28^o21'27''$ were performed by using IRAM 30-m radiotelescope (Granada, Spain). The observations were gathered in three observational campaigns during 2019 (April 10–16, August 13–19, and December 11–15) and were part of the projects 172–18 (PI Martín-Pintado), 018–19, and 133–19 (PI Rivilla), respectively. Observations were conducted using position switching mode, with the off position located at an offset of $\Delta\alpha = -885$ arcsec and $\Delta\delta = 290$ arcsec. The broad-band heterodyne Eight MIxer Receiver and the Fast Fourier Transform Spectrometer FTS200 were used, which provided a raw frequency resolution of ∼200 kHz. In this work, we used data covering the spectral ranges 71.8–116.7 and 124.8–175.5 GHz. We smoothed the spectra achieving a final resolution of ∼800 kHz (1.4–3.3 km s^{-1}), which is sufficient to resolve G+0.693 molecular line profiles that present typical line widths of ∼15–25 km s^{-1}. The telescope beamwidth varies from ∼34.2 arcsec at 72 GHz up to ∼14.0 arcsec at 176 GHz. The line intensity of the spectra was measured in antenna temperature, T_A^*, units, as the molecular emission towards G+0.693 is extended over the beam (e.g. Zeng et al. 2020). More details of the observations are provided in Rivilla et al. (2021a, b, 2022b).

3 ANALYSIS AND RESULTS

The identification of H_2CN and H_2NC molecular lines and their fitting have been performed using the version from 2021 March 3 of the Spectral Line Identification and Modelling (SLIM) tool within the MADCUBA[2] package (Martín et al. 2019). SLIM generates a synthetic spectrum under the assumption of local thermodynamic equilibrium (LTE) conditions, to be compared with the observed one. Then, an autofitting procedure, SLIM-AUTOFIT, provides the best non-linear least-squares LTE fit to the data using the Levenberg–Marquardt algorithm. The free parameters used for the fit procedure are the total column density of the molecule (N), the excitation temperature (T_{ex}), the local standard of rest velocity (v_{LSR}), and the full width at half maximum (FWHM).

For the analysis, we have used the Cologne Database for Molecular Spectroscopy (CDMS; Endres et al. 2016) spectroscopic entries 028502 (2000 July) for H_2CN and 028528 (2021 September) for H_2NC, which were obtained from Yamamoto & Saito (1992) and Cabezas et al. (2021), respectively. The dipole moment of H_2CN was obtained from *ab initio* calculation by Cowles et al. (1991), while that of H_2NC comes from a quantum chemical calculation from the work by Cabezas et al. (2021). To perform the LTE line fitting, we have used the most unblended transitions of each molecule, along with those partially blended with lines from other molecular species previously identified and modelled towards G+0.693.

3.1 Detection of H_2NC

We show in Fig. 1 all the H_2NC transitions detected towards G+0.693 (purple vertical lines of Fig. 1), consisting of the hyperfine structures of the $N_{K_aK_c} = 1_{01}$–0_{00} and 2_{02}–1_{01} rotational transitions, with upper energy levels of 3.5 and 10.4 K, respectively. Only transitions with intensities $T_A^* > \sigma/3$ (where σ is the rms of the spectra) are considered to compute the synthetic spectrum. The spectroscopic information of the observed transitions is shown in Appendix A. The pattern produced by all these hyperfine components creates a very characteristic spectral line profile, which reproduces very nicely the observed spectrum, confirming the presence of this molecule in G+0.693. All of the transitions are unblended from emission of other species, except those falling in the 72.19–72.20 GHz range, which are blended with $H_2CCCHCN$, CCD, and C_2H_3CN (see Fig. 1). The global fit including all species properly matches the observed spectrum.

The LTE AUTOFIT procedure for H_2NC was carried out by using all its detected transitions and leaving all four parameters free, obtaining $N = (4.2 \pm 0.7) \times 10^{12}$ cm^{-2}, $T_{ex} = 3.28 \pm 0.11$ K, $v_{LSR} = 71.0 \pm 0.5$ km s^{-1}, and FWHM $= 18.3 \pm 1.1$ km s^{-1} (see Table 1). As expected, the derived T_{ex} is much lower than the T_{kin} of the source (∼70–140 K; Zeng et al. 2018), and similar to that derived for chemically similar species such as the HCN and HNC isotopologues (Colzi et al. 2022), or other species such as PN (Rivilla et al. 2022a). Higher values of T_{ex} (5–10 K) do not properly fit both rotational transitions of H_2NC, but significantly overestimate the 2_{02}–1_{01} transitions.

We have derived the molecular abundance of H_2NC with respect to H_2, using $N_{H_2} = 1.35 \times 10^{23}$ cm^{-2} from Martín et al. (2008) and assuming an uncertainty of 15 per cent to its value, as done in Rodríguez-Almeida et al. (2021a). The resulting abundance is $(3.1 \pm 0.7) \times 10^{-11}$ (see Table 1).

3.2 Detection of H_2CN

The hyperfine structures of the 1_{01}–0_{00} and 2_{02}–1_{01} rotational transitions have also been detected for H_2CN for the first time towards

[2]Madrid Data Cube Analysis on ImageJ is a software developed at the Centre of Astrobiology (CAB) in Madrid: https://cab.inta-csic.es/madcuba.

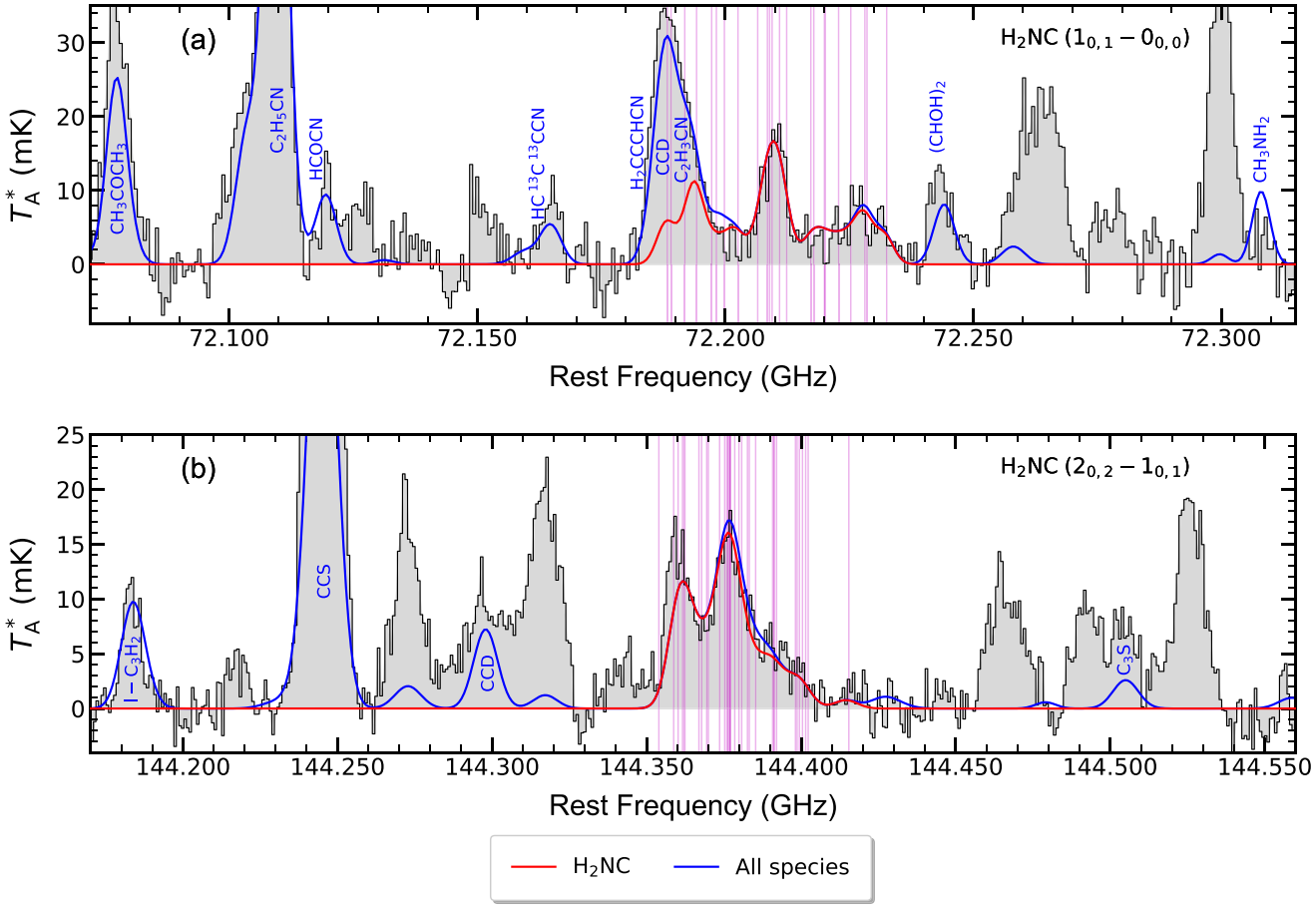

Figure 1. H_2NC hyperfine lines observed towards G+0.693, corresponding to the 1_{01}–0_{00} rotational transition (upper panel) and the 2_{02}–1_{01} rotational transition (lower panel). Black histogram and grey-shaded areas indicate the observed spectrum, while the red and blue lines represent the best LTE fit obtained for H_2NC and the emission of all the species already identified in the cloud (whose names are indicated by the blue labels), respectively. Magenta vertical lines indicate those transitions selected to perform the AUTOFIT. The transitions shown are only those with peak intensities of $T_A^* > 0.41$ mK, which correspond to $\sigma/3$ value (where σ is the rms of the spectra). The spectroscopic information for the observed transitions is given in Appendix A.

Table 1. Physical parameters derived by the LTE best fit for H_2CN and H_2NC. The parameters assumed in the fit procedure are shown without errors, as explained in Section 3.1 for H_2NC and Section 3.2 for H_2CN. The fractional abundances with respect to H_2 are shown in the last column. Uncertainties correspond to 1σ standard deviations, except for N_{H_2}, which is assumed to be 15 per cent of its value.

Molecule	N ($\times 10^{12}$ cm^{-2})	T_{ex} (K)	FWHM (km s^{-1})	v_{LSR} (km s^{-1})	N/N_{H_2} ($\times 10^{-11}$)
H_2NC	4.2 ± 0.7	3.28 ± 0.11	18.3 ± 1.1	71.0 ± 0.5	3.1 ± 0.7
H_2CN	9.2 ± 1.1	3.28	18.3	71.0	6.8 ± 1.3

Note. We have used the N_{H_2} value derived by Martín et al. (2008) of 1.35×10^{23} cm^{-2}.

G+0.693, as shown in Fig. 2. The two H_2CN rotational transitions observed present upper energy levels of 3.5 and 10.6 K, respectively (upper and lower panels of Fig. 2). As in the case of H_2NC, only transitions with intensities $T_A^* > \sigma/3$ are considered to compute the synthetic spectrum. The spectroscopic information of H_2CN detected lines can be found in Appendix A.

In contrast to the H_2NC detected lines (Fig. 1), most of H_2CN transitions are highly blended with transitions from other species already identified, mainly C_2H_5CN, $NH_2CH_2CH_2OH$, and CH_3OCH_3 (see Fig. 2). Four hyperfine H_2CN transitions at 73.369, 73.393, 73.395, and 73.444 GHz are completely unblended (magenta vertical lines in Fig. 2), and we have used them to perform AUTOFIT. Since all of them have the same energy levels, the AUTOFIT procedure does not converge when leaving free the T_{ex}. We have checked how different assumed values of T_{ex} affect the LTE synthetic spectrum of the higher energy 2_{02}–1_{01} lines. We found that T_{ex} should be indeed close to 3 K, similar to H_2NC, since higher temperatures clearly overestimate the 2_{02}–1_{01} transitions (see Appendix B). Hence, we have confidently used the T_{ex} estimated for H_2NC (3.28 K) to perform the fit of H_2CN. Similarly, we also fixed v_{LSR} to 71.0 km s^{-1} and the FWHM to 18.3 km s^{-1}, as derived for H_2NC. The AUTOFIT procedure derives $N = (9.2 \pm 1.1) \times 10^{12}$ cm^{-2}. The corresponding H_2CN molecular abundance relative to H_2 is $(6.8 \pm 1.3) \times 10^{-11}$ (see Table 1).

3.3 The H_2CN/H_2NC abundance ratio towards G+0.693

Based on the column density estimates, we have obtained an H_2CN/H_2NC ratio of 2.2 ± 0.5 towards G+0.693. This ratio is well above 1, consistent within uncertainty to what was found for the warm gas towards the galaxy at $z = 0.89$ in front of PKS 1830−211 (3.7 ± 1.1; Cabezas et al. 2021). In our analysis, the isomeric ratio has been derived using the same T_{ex} for both molecules (3.28 K), as Cabezas et al. (2021) and Agundez et al. (2023) also did for the

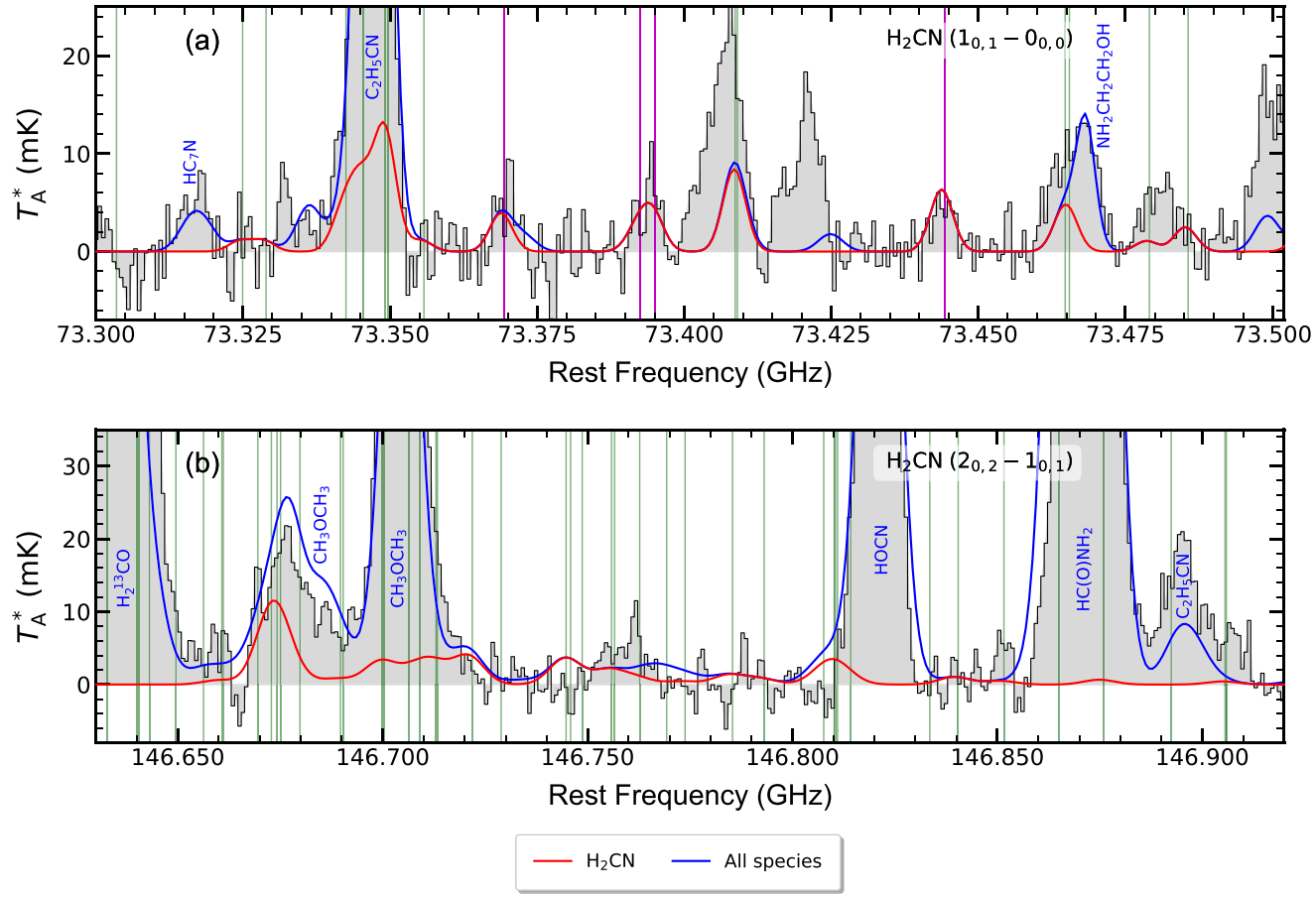

Figure 2. Same as Fig. 1, but for H_2CN. Green vertical lines indicate other H_2CN transitions that were not used in the fit (see text). The spectroscopic information for all of the observed transitions is given in Appendix A.

other sources. We note that this low excitation temperature is very similar to that derived by the Cabezas et al. (2021) for L483 and B1-b. We have also evaluated how the H_2CN/H_2NC ratio varies assuming different T_{ex} values for H_2CN, while keeping fixed the T_{ex} of H_2NC to 3.28 K as derived from its fit. Since we have already demonstrated that the T_{ex} of H_2CN should be close to 3 K and cannot be >4 K (as indicated in Appendix B), we have varied T_{ex} within the 2σ confidence level of the fit of H_2NC, i.e. ∼3.0–3.5 K. We have found that the H_2CN/H_2NC abundance ratio ranges between 1.7 and 3.0, remaining unchanged with respect to the original estimate and errors.

4 DISCUSSION

4.1 The H_2CN/H_2NC abundance ratio behaviour with T_{kin}

The G+0.693 molecular cloud is the first warm galactic molecular cloud and the second warm interstellar source, after the $z = 0.89$ galaxy in front of PKS 1830−211 (Tercero et al. 2020), where both the H_2CN and H_2NC isomers have been detected. The H_2CN/H_2NC ratio we have derived towards G+0.693, 2.2 ± 0.5, along with that previously derived for PKS 1830−211 (3.7 ± 1.1), confirms that this isomeric ratio in warm gas is higher than that found in cold dense clouds (T_{kin} ∼ 10 K), where it is ∼1.

We show in Fig. 3 the dependence of the H_2CN/H_2NC ratio on T_{kin}. For G+0.693, we have considered $T_{kin} > 70$ K, since Zeng et al. (2018) found that T_{kin} ranges between ∼70 and ∼140 K by analysing the *K*-ladders of different rotational transitions of CH_3CN, which is in good agreement with the values derived using NH_3 towards Galactic Centre molecular clouds (Guesten et al. 1985; Huettemeister et al. 1993; Krieger et al. 2017). In the case of PKS 1830−211, we have adopted the lower limit of ≳80 K derived by Henkel et al. (2008) using NH_3 absorption.

To compute the uncertainties of the isomeric ratios for which these were not provided, we have used the integrated intensity uncertainties resulting from the published line fitting. For each cold source, we have used the following T_{kin}: 9.5 ± 0.3 K for L483 [from NH_3 and CO emission, Anglada et al. (1997) and Tafalla et al. (2000), respectively], 12 ± 2 K for B1-b (from CO emission; Bachiller & Cernicharo 1984; Marcelino et al. 2005), ∼10 K for TMC-2 (from HC_5N emission; Benson & Myers 1983), 9.9 ± 0.5 K for L134N (from NH_3 emission; Dickens et al. 2000), 12.5 ± 0.2 K for Lupus-1A (based also on NH_3 emission; Benedettini et al. 2012), 13 ± 1 K for L1489 (using CH_3CCH emission; Wu et al. 2019), and 7.5 K with a 1σ confidence range of 5–12 K for L1544 [as Bianchi et al. (2023) estimated from HC_5N, HC_7N, and HC_9N emission].

Fig. 3 hints a clear dependence between the H_2CN/H_2NC abundance ratio and T_{kin}, with ratios above 2 for the warmer sources (G+0.693 and PKS 1830−211). On the other hand, the average value of this ratio found towards the seven cold clouds is 1.2 ± 0.6. The ratios derived for these objects range between 0.6 and 1.5, with the only exception of TMC-2 (Fig. 3), which shows the largest uncertainty.

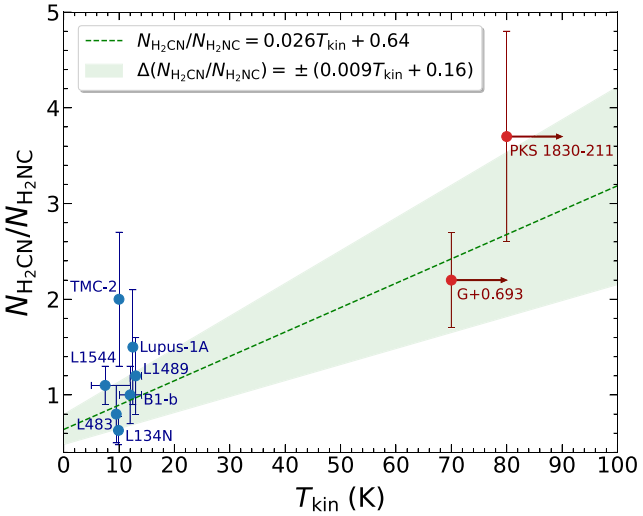

Figure 3. H_2CN/H_2NC abundance ratio versus T_{kin}. Blue and red points are associated with cold ($T_{kin} \sim 10$ K) and warm ($T_{kin} > 70$ K) sources. The dashed green line traces the linear fit shown in equation (1), while the green shaded region encompasses the 1σ of uncertainty on the linear regression fit. The T_{kin} of G+0.693 is assumed to be >70 K from CH_3CN observations performed by Zeng et al. (2018). The rest of T_{kin} values were taken from Anglada, Sepulveda & Gomez (1997) and Tafalla et al. (2000) for L483, from Marcelino et al. (2005) for B1-b, from Henkel et al. (2008) for PKS 1830−211, and from Benson & Myers (1983), Dickens et al. (2000), Benedettini et al. (2012), Wu et al. (2019), and Bianchi et al. (2023) for TMC-2, L134N, Lupus-1A, L1489, and L1544, respectively. The H_2CN/H_2NC ratios of the sources not studied in this work were taken from Cabezas et al. (2021) and Agundez et al. (2023).

Therefore, the H_2CN/H_2NC ratio increases at higher T_{kin}, similar to what was found for the HCN/HNC abundance ratio (e.g. Hacar et al. 2020). Considering a T_{kin} of 70 K for G+0.693, we performed a weighted linear regression fit, which is presented with a green dashed line in Fig. 3 and accounts for uncertainties, yielding

$$\frac{H_2CN}{H_2NC} \equiv \frac{N_{H_2CN}}{N_{H_2NC}} = (0.026 \pm 0.009)\, T_{kin} + (0.64 \pm 0.16)\,. \quad (1)$$

In contrast to the HCN/HNC ratio relation with T_{kin} found by Hacar et al. (2020) for HCN/HNC ratios $\leq$4 ($T_{kin} = 10 \times$ HCN/HNC or, equivalently, HCN/HNC = 0.1 T_{kin}), the correlation we have found for the H_2CN/H_2NC ratio has a shallower slope of 0.026. This indicates that the H_2CN/H_2NC ratio, although dependent on T_{kin}, seems to be less sensitive to it than the HCN/HNC ratio. As this value is in fact an upper limit for the slope, these conclusions still hold if a T_{kin} of ∼140 K [the highest value in the temperature range derived by Zeng et al. (2018)] is adopted for G+0.693, in which case a slope of 0.012 is obtained. In any case, we note that the trend found for the H_2CN/H_2NC ratio is still based on only two warm interstellar sources, and more detections of this isomeric pair towards other regions, covering sources with high ($T_{kin} > 70$ K) and also intermediate temperatures (10 K < T_{kin} < 70 K), would help to better describe the trend with the temperature.

4.2 Interstellar chemistry of H_2CN and H_2NC

The origin of the observed H_2CN/H_2NC abundance ratios and their possible link with the gas T_{kin} can be related to different physical conditions or chemical processes, which can take place both in the gas phase and/or in the ices covering the interstellar dust grains. For

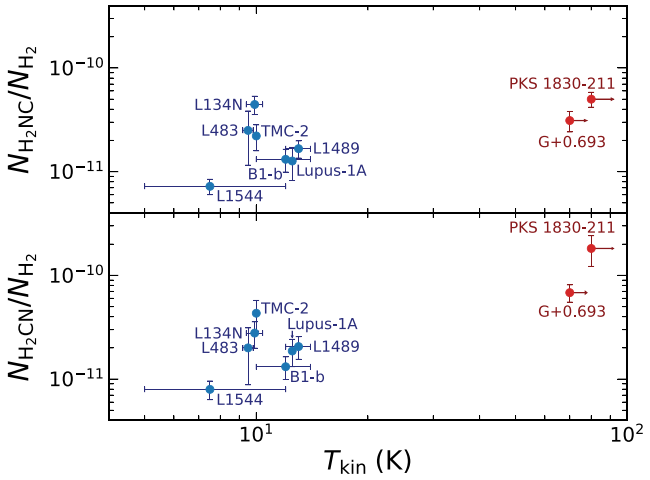

Figure 4. H_2NC (upper panel) and H_2CN (lower panel) molecular abundances relative to H_2 versus the gas kinetic temperature. Blue and red colours are associated with the cold ($T_{kin} \sim 10$ K) and warm ($T_{kin} > 70$ K) sources, respectively. H_2CN and H_2NC molecular abundances come from this work and Cabezas et al. (2021) and Agundez et al. (2023). The H_2 column density of G+0.693 is $(1.4 \pm 0.2) \times 10^{23}$ cm^{-2} (Martín et al. 2008), while for the rest of the sources are $(2.2 \pm 0.3) \times 10^{22}$ cm^{-2} (PKS 1830−211; Muller et al. 2014), $(4.0 \pm 2.0) \times 10^{22}$ cm^{-2} (L483; Agúndez et al. 2019), $(7.6 \pm 1.1) \times 10^{22}$ cm^{-2} (B1-b; Daniel et al. 2013), $(9.5 \pm 1.4) \times 10^{21}$ cm^{-2} (TMC-2; Turner, Pirogov & Minh 1997), $(9.0 \pm 1.4) \times 10^{21}$ cm^{-2} (L134N; Dickens et al. 2000), $(1.50 \pm 0.23) \times 10^{22}$ cm^{-2} (Lupus-1A; Agúndez, Cernicharo & Guélin 2015), $(1.02 \pm 0.07) \times 10^{22}$ cm^{-2} (L1489; Wu et al. 2019), and $(5.4 \pm 0.8) \times 10^{22}$ cm^{-2} (L1544; Jiménez-Serra et al. 2016). When not given, uncertainties of $N(H_2)$ were adopted to be 15 per cent of the value.

example, it has been shown that the HCN/HNC ratio might depend on the collisional excitation of these molecules with He (Sarrasin et al. 2010; Hays et al. 2022), on the increase of the cosmic ray ionization rate in high-temperature environments (∼100 K; Behrens et al. 2022), on the isomerization of HNC into HCN in the icy dust grain surfaces (Baiano et al. 2022), on the ultraviolet radiation field (Bublitz et al. 2022), and on the kinetic temperature (Jin, Lee & Kim 2015; Colzi et al. 2018; Hacar et al. 2020; Pazukhin et al. 2022). Motivated by the trend found in Section 4.1, we focus here on the possible dependence of the H_2CN/H_2NC ratio on T_{kin}, discussing possible chemical reactions forming and destroying these two radicals.

Unlike H_2CN, the chemistry of H_2NC is very poorly explored, since it is missing in chemical kinetic data bases commonly used in astrochemistry, such as UDfA (UMIST Database for Astrochemistry; McElroy et al. 2013) or KIDA (KInetic Database for Astrochemistry; Wakelam et al. 2012). Moreover, the predominant detection of these two isomers in cold clouds, which are expected to be mainly affected by gas-phase chemistry, has only triggered the study of different gas-phase chemical routes. None the less, chemical pathways occurring on the ices covering dust grains can be especially important in the case of G+0.693, where the presence of shocks is able to inject the molecules into the gas phase, or in warm sources such as PKS 1830−211, where thermal and shock-induced desorptions are also possible (Tercero et al. 2020; Muller et al. 2021). To explore this hypothesis, we have computed the molecular abundances of both H_2CN and H_2NC isomers with respect to H_2 for all of the sources, and analysed their dependence on the gas T_{kin} (see Fig. 4). The H_2 column densities of those objects not studied in this work were obtained from various studies [Muller et al. (2014) for PKS 1830−211, Agúndez et al. (2019) for L483, Daniel et al. (2013) for B1-b, Turner et al. (1997) for TMC-2, Dickens et al. (2000) for L134N, Agúndez et al.

(2015) for Lupus-1A, Wu et al. (2019) for L1489, and Jiménez-Serra et al. (2016) for L1544], and range from $\sim 1 \times 10^{22}$ to $\sim 8 \times 10^{22}$ cm^{-2}. An uncertainty of 15 per cent of their value was assumed when not provided, as done for G+0.693. In the case of TMC-2 and L134N, H_2 volume density was converted into column density by assuming spherical geometry and using the source size provided by the corresponding above-mentioned works.

As Fig. 4 illustrates, both the warm/shocked sources (G+0.693 and PKS 1830−211) exhibit higher abundances of H_2CN, which are up to an order of magnitude larger than those observed in most of the cold clouds. H_2NC appears also to be more abundant in these two warm objects, albeit the difference with respect to the cold sources is not as significant. These findings suggest that surface chemistry might be enhancing both H_2NC and, more notably, H_2CN abundances in warm/shocked environments.

In the next sections, we discuss the possible gas-phase formation and destruction routes that have been studied so far for H_2CN (Cimas & Largo 2006; Holzmeier et al. 2013; Bourgalais et al. 2015) and H_2NC (Cabezas et al. 2021; Agundez et al. 2023). Moreover, we also propose alternative pathways that might occur on the surface of the ices, which can potentially enhance their abundances in warm and/or shocked regions.

4.2.1 *H_2CN and H_2NC formation mechanisms*

A first H_2CN formation route occurs through the gas-phase reaction $CH_3 + N(^4S) \rightarrow H_2CN + H$, which was studied experimentally by Marston, Nesbitt & Stief (1989), and also computationally by Cimas & Largo (2006) through calculations at the CCSD(T)/cc-pVTZ, MP2/CBS, B3LYP/CBS, and G2 levels of theory. Cimas & Largo (2006) showed that this reaction first gives H_3CN as an intermediate species, which subsequently forms H_2CN with a branching ratio of ∼0.997[3]. They also considered the formation of H_2NC (with a negligible branching ratio of $\sim 10^{-5}$) and *trans*-HCNH (branching ratio of ∼0.0025). All these processes are exothermic and barrierless, and H_2CN is the main product being the most favourable pathway both thermodynamically and kinetically. Cimas & Largo (2006) also analysed the formation of HCN (branching ratio of ∼0.185[4]) and HNC (∼0.071) through the same reaction, but starting with atomic N in an excited state (^2D). Although the formation of HCN and HNC is thermodynamically favoured, these molecules are not the preferred products from the kinetic point of view, as their transition states lie higher in energy than those for H_2CN. Therefore, H_2CN is the main product of this reaction with a branching ratio of ∼0.745, although the formation of HCN and HNC is also possible. However, this reaction will not occur in the ISM since the population of excited $N(^2D)$ atoms is going to be negligible with respect to that of $N(^4S)$ atoms.

Another possible H_2CN formation route involves the gas-phase reaction of $C + NH_3 \rightarrow H_2CN + H$, which was initially studied by Bourgalais et al. (2015) through both experiments and theoretical calculations at the MRCI+Q/aug-cc-pVQZ, CCSD(T)/aug-cc-pVQZ, and M06-2X/cc-pVQZ levels. Bourgalais et al. (2015) reported that the $H_2CN + H$ exit channel represents about 100 per cent of the product yield for this reaction (branching ratio ≃1), being an exothermic reaction that occurs without an emerged barrier. They also showed that the exothermic channels that lead to HCN + 2H or HNC + 2H are final minor products. However, although Bourgalais et al. (2015) did not discuss the formation of H_2NC, Cabezas et al. (2021) argued that it could also take place through the $C + NH_3$ reaction. This is because it first involves the formation of the CNH_3 intermediate species in a barrierless process, which followed by the elimination of an H atom would directly lead to $H_2NC + H$ [similar to the most favoured path of the $CH_3 + N$ reaction from Cimas & Largo (2006), which first involves the formation of H_3CN]. Moreover, the chemical structure of the intermediate species CNH_3 could also favour the formation of H_2NC instead of H_2CN, in which significant atomic rearrangement is required. More recently, Agundez et al. (2023) revisited this reaction theoretically and found that both H_2CN and H_2NC can be formed in an exothermic process. Their calculations using the RCCSD(T)-F12, MRCI-F12, and MRCI-F12+Q methods in combination with the cc-pVQZ-F12 and cc-pVTZ-F12 basis sets, showed that the CNH_3 intermediate species could first evolve towards two transition states very close in energy, but located below the reactants. The highest energy transition state would directly lead to $H_2NC + H$ products in a barrierless process, while the $H_2CN + H$ exit channel would be favoured by means of a statistical mechanism starting from the lowest energy transition state, and consequently going through different reaction intermediates. Agundez et al. (2023) predicted that the H_2CN/H_2NC ratio at low temperatures (10 K) has a value between 1.25 and 2, reasonably similar to the values observed in the cold molecular clouds (see Fig. 3). However, the absence of an entrance barrier makes this reaction not temperature-dependent, thus preventing it from explaining the higher ratios and molecular abundances found towards the warm sources. Although it might be a dominant formation route of both isomers in the gas phase, it is not responsible for the H_2CN/H_2NC abundance ratio dependence on temperature found.

Talbi & Ellinger (1996) also studied the formation of H_2CN and H_2NC via HCN + H and HNC + H gas-phase reactions. However, in addition to the fact that forming a single product from a two-body reaction makes it highly unstable, their high activation barriers of ∼15.2 kcal mol^{-1} (∼7700 K) and ∼19.2 kcal mol^{-1} (∼9700 K) make these processes highly inefficient at the conditions of the ISM.

The detection of H_2CN and H_2NC towards the G+0.693 molecular cloud, whose chemistry is dominated by shock-induced desorption (Rivilla et al. 2020, 2021a, 2022b), led us to consider also grain surface chemistry. Possible formation routes might be one H-atom addition through the direct hydrogenation of HCN and HNC, respectively, on the surface of dust grains. Theule et al. (2011) performed hydrogenation experiments of pure HCN ices, and found that they fully hydrogenate into methylamine (CH_3NH_2). In this process, H_2CN is a non-stable intermediate species. However, we note that the H-atom flux in the experiments is likely much higher than that in the ISM conditions, where the survival of intermediate species is then favoured, although at much lower abundances than the parent species. In G+0.693, the HCN/H_2CN ratio is indeed $(5.0 \pm 0.6) \times 10^3$ [using the column density reported here and in Colzi et al. (2022)], in agreement with this hypothesis. In a similar way, H_2NC might be formed on grains through the hydrogenation of HNC, but to our best knowledge there are no laboratory experiments that have specifically studied this process. The detections of H_2CN and H_2NC in shock-dominated and/or thermal-dominated sources like G+0.693 and PKS 1830−211 impose the need of exploring in more detail their chemistry on the surface of ices, both in the laboratory and also by dedicated quantum chemical calculations.

[3]Modification of the temperature in the range 100–500 K alters these branching ratios only in the fourth decimal figure towards the formation of H_2CN and trans-HCNH, but remains constant for H_2NC.
[4]Modification of the temperature in the range 100–500 K alters these branching ratios only in the third decimal figure.

4.2.2 H_2CN and H_2NC destruction mechanisms

Given that it has been proposed that the dependence of the HCN/HNC ratio on T_{kin} is mainly due to destruction and isomerization mechanisms (Lin, He & Melius 1992; Talbi & Ellinger 1996; Graninger et al. 2014; Jin et al. 2015; Hacar et al. 2020), it is also worth to explore possible destruction pathways for the H_2CN and H_2NC isomers. However, the destruction of these two isomers has been poorly studied so far. In the case of H_2CN, to our best knowledge, the only destruction routes proposed in the literature are gas-phase reactions with neutral H, C, N, and O atoms, which were summarized by Loison, Wakelam & Hickson (2014), based on previous works by Fikri et al. (2001), Cho & Andrews (2011), or Hébrard et al. (2012) among others.

The $H_2CN + H$ destruction reaction was first studied experimentally by Nesbitt, Marston & Stief (1990), who derived a lower limit for its rate constant. Through *ab initio* calculations at the M06-2X/cc-pVTZ and MRCI+Q/cc-pVQZ levels, Hébrard et al. (2012) determined that this reaction can give HCN + H_2 or HNC + H_2 as final products in an exothermic process without entrance barrier. Based on statistical calculations, they estimated that 20 per cent of the total production goes into HNC formation, while 80 per cent into HCN.

Regarding the $H_2CN + N$ reaction, Nesbitt et al. (1990) determined its rate constant (at temperatures in the range 200–363 K) with large uncertainties, so that extrapolation to lower temperatures would be unreliable. To form the products NH + HCN, an emerged barrier of ∼1320 K should be overcome (Cimas & Largo 2006), and it is not expected to occur under interstellar conditions. The preferable products of the reaction are then CH_2 + N2 due to the absence of a barrier, as found by Hébrard et al. (2012) from *ab initio* calculations at the M06-2X/cc-pVTZ level.

The $H_2CN + C$ and $H_2CN + O$ reactions have not been specifically studied experimentally or theoretically. Loison et al. (2014) estimated their parameters by analysing similar chemical reactions (Lau et al. 1999; Fikri et al. 2001; Koput 2003; Osamura & Petrie 2004; Zhang, Du & Feng 2004; Cho & Andrews 2011). We note that special attention should be paid to $H_2CN + O$ and $H_2NC + O$ reactions, as it has been shown that the reaction HNC + O could be the dominant mechanism producing the observed HCN/HNC, because the same reaction is unable to occur for HCN under ISM temperature conditions (Lin et al. 1992). In a very similar way, the destruction reaction HNC + H has been proposed to be an efficient mechanism converting HNC into HCN (Pineau des Forets, Roueff & Flower 1990; Talbi & Ellinger 1996; Jin et al. 2015; Hacar et al. 2020), so that the destruction reactions $H_2CN + H$ and $H_2NC + H$ might also deserve special consideration. Thus, taking the HNC and HCN isomeric pair as a reference, it would be interesting to analyse theoretically and experimentally the differences in H_2CN and H_2NC destruction reactions with atomic O and H, and their dependence on T_{kin}, which might be able to explain the observed trend of the H_2CN/H_2NC ratio (Section 4.1).

Moreover, a temperature dependence of the gas-phase isomerization of H_2NC into H_2CN would be another way to explain the observed H_2CN/H_2NC abundance ratio dependence on T_{kin}. However, Holzmeier et al. (2013) argued that the isomerization cannot occur in either direction in gas phase, due to the large difference in energy between these two isomers in their ground state (∼12 000 K or ∼24 kcal mol^{-1}), and the even higher energy barriers within the isomerization process itself (∼23 000 K). These large barriers cannot be overcome under typical molecular ISM conditions (T_{kin} ∼ 10–100 K), even considering quantum tunnelling effects. Notwithstanding, since quantum tunnelling probability strongly depends on the shape and width of the reaction barriers, a more detailed analysis of this reaction would be required. In any case, a very high degree of atom rearrangement is needed to form H_2NC from H_2CN and vice versa, which also makes isomerization very unlikely.

Regarding surface chemistry, as noted above, reactions involving H_2NC from H_2CN are poorly studied. Besides the H-atom addition mentioned before, which would destroy them to form more saturated species such as methanimine and methylamine [as shown in the experiments by Theule et al. (2011)], it would be worth to study the possible surface isomerization $H_2CN \rightleftharpoons H_2NC$. Baiano et al. (2022) demonstrated that a similar surface isomerization process between HNC and HCN is possible in the presence of water molecules. They formed HCN from HNC in the presence of H_2O molecules through quantum tunnelling effects, with a reaction rate that increases with the temperature. If an analogous process is also possible for H_2CN and H_2NC, this would already increase the H_2CN/H_2NC isomeric ratio on ices, which would be inherited by the gas phase after desorption (both shock-induced or thermal). This mechanism, which needs to be studied, might be able to naturally explain the higher H_2CN/H_2NC ratio found towards G+0.693 and PKS 1830−211.

5 CONCLUSIONS

We have reported for the first time the detection of H_2CN and its high-energy metastable isomer H_2NC towards a warm (T_{kin} > 70 K) galactic molecular cloud, G+0.693, which is located in the Galactic Centre of our Galaxy. Using IRAM 30-m telescope observations, we have detected several hyperfine components of the $N_{K_aK_c} = 1_{01}–0_{00}$ and $2_{02}–1_{01}$ transitions. We performed an LTE fit to the observed spectra, deriving $N = (4.2 \pm 0.7) \times 10^{12}$ cm^{-2} and $T_{ex} = 3.28 \pm 0.11$ K for H_2NC, and $N = (9.2 \pm 1.1) \times 10^{12}$ cm^{-2} when assuming $T_{ex} = 3.28$ K for H_2CN. Therefore, we have derived molecular abundances with respect to H_2 of $(6.8 \pm 1.3) \times 10^{-11}$ for H_2CN and of $(3.1 \pm 0.7) \times 10^{-11}$ for H_2NC, and an isomeric abundance ratio of $H_2CN/H_2NC = 2.2 \pm 0.5$. This result, along with the ratio previously found towards the $T_{kin} \gtrsim 80$ K gas of a $z = 0.89$ galaxy in front of the quasar PKS 1830−211 (3.7 ± 1.1), confirms that the H_2CN/H_2NC ratio is higher in warm sources than in cold (T_{kin} ∼ 10 K) clouds, where it is ∼1. This suggests that, similar to the HCN/HNC ratio, the H_2CN/H_2NC abundance ratio can also be used as a new potential temperature tracer for the ISM. We have found that the dependence of the H_2CN/H_2NC isomeric ratio on T_{kin} is shallower (∼$0.026T_{kin}$) than that previously found for the HCN/HNC ratio (∼$0.1T_{kin}$). The observed dependence of the H_2CN/H_2NC ratio on the gas T_{kin} cannot be fully explained only with the current proposed formation and destruction pathways in the gas phase, although the latter should be studied in more detail. In particular, the higher ratios and molecular abundances (up to one order of magnitude larger in the case of H_2CN) found in G+0.693 (where shock-induced desorption dominates) and PKS 1830−211 (where thermal desorption is also possible), impose the need of considering also surface chemistry on the icy grain mantles. Hence, the observational result presented here highlights the importance of performing new laboratory experiments and quantum chemical calculations to study, e.g. the surface formation of H_2CN and H_2NC through the direct hydrogenation of HCN and HNC, respectively, their destruction by subsequent H-atom additions, or their possible isomerization on the ices, as previously proposed for HCN and HNC. These mechanisms can introduce an isomeric preference

on ices, which later on would be inherited in the gas phase in those sources where shocks or heating can desorb the molecules. This might contribute to explain the higher H_2CN/H_2NC values derived towards G+0.693 and PKS 1830−211, compared to cold molecular clouds where pure gas-phase chemistry is expected to dominate.

ACKNOWLEDGEMENTS

We are very grateful to the IRAM 30-m telescope staff for their precious help during the different observing runs. We acknowledge Germán Molpeceres for enlightening discussions about the surface chemistry of the species studied in this work. DSA acknowledges the funds provided by the Consejo Superior de Investigaciones Científicas (CSIC) and the Centro de Astrobiología (CAB) through the project 20225AT015 (Proyectos intramurales especiales del CSIC). LC, IJ-S, and JM-P acknowledge financial support through the Spanish grant PID2019-105552RB-C41 funded by the Spanish Ministerio de Ciencia e Innovación and the Spanish State Research Agency (MCIN/AEI/10.13039/501100011033). VMR has received support from the project RYC2020-029387-I funded by the Spanish Ministerio de Ciencia e Innovación and the Spanish State Research Agency (MCIN/AEI/10.13039/501100011033), and from the Comunidad de Madrid through the Atracción de Talento Investigador Modalidad 1 (Doctores con experiencia) Grant (COOL: Cosmic Origins Of Life; 2019-T1/TIC-5379).

DATA AVAILABILITY

The data underlying this article will be shared on reasonable request to vrivilla@cab.inta-csic.es.

REFERENCES

Agúndez M., Cernicharo J., Guélin M., 2015, A&A, 577, L5
Agúndez M., Marcelino N., Cernicharo J., Roueff E., Tafalla M., 2019, A&A, 625, A147
Agundez M., Roncero O., Marcelino N., Cabezas C., Tercero B., Cernicharo J., 2023, A&A, 673, A24
Anglada G., Sepulveda I., Gomez J. F., 1997, A&AS, 121, 255
Bachiller R., Cernicharo J., 1984, A&A, 140, 414
Baiano C., Lupi J., Barone V., Tasinato N., 2022, J. Chem. Theory Comput., 18, 3111
Behrens E. et al., 2022, ApJ, 939, 119
Benedettini M., Pezzuto S., Burton M. G., Viti S., Molinari S., Caselli P., Testi L., 2012, MNRAS, 419, 238
Benson P. J., Myers P. C., 1983, ApJ, 270, 589
Bianchi E. et al., 2023, ApJ, 944, 208
Bourgalais J. et al., 2015, ApJ, 812, 106
Bublitz J., Kastner J. H., Hily-Blant P., Forveille T., Santander-García M., Alcolea J., Bujarrabal V., 2022, A&A, 659, A197
Cabezas C., Agúndez M., Marcelino N., Tercero B., Cuadrado S., Cernicharo J., 2021, A&A, 654, A45
Chantzos J., Rivilla V. M., Vasyunin A., Redaelli E., Bizzocchi L., Fontani F., Caselli P., 2020, A&A, 633, A54
Cho H.-G., Andrews L., 2011, J. Phys. Chem. A, 115, 8638
Cimas A., Largo A., 2006, J. Phys. Chem. A, 110, 10912
Colzi L., Fontani F., Caselli P., Ceccarelli C., Hily-Blant P., Bizzocchi L., 2018, A&A, 609, A129
Colzi L. et al., 2022, ApJ, 926, L22
Cowles D. C., Travers M. J., Frueh J. L., Ellison G. B., 1991, J. Chem. Phys., 94, 3517
Daniel F. et al., 2013, A&A, 560, A3
Dickens J. E., Irvine W. M., Snell R. L., Bergin E. A., Schloerb F. P., Pratap P., Miralles M. P., 2000, ApJ, 542, 870
Endres C. P., Schlemmer S., Schilke P., Stutzki J., Müller H. S. P., 2016, J. Mol. Spectrosc., 327, 95
Fikri M., Meyer S., Roggenbuck J., Temps F., 2001, Faraday Discuss., 119, 223
Graninger D. M., Herbst E., Öberg K. I., Vasyunin A. I., 2014, ApJ, 787, 74
Guesten R., Walmsley C. M., Ungerechts H., Churchwell E., 1985, A&A, 142, 381
Hacar A., Bosman A. D., van Dishoeck E. F., 2020, A&A, 635, A4
Hays B. M., Gupta D., Guillaume T., Abdelkader Khedaoui O., Cooke I. R., Thibault F., Lique F., Sims I. R., 2022, Nat. Chem., 14, 811
Hébrard E., Dobrijevic M., Loison J. C., Bergeat A., Hickson K. M., 2012, A&A, 541, A21
Henkel C., Braatz J. A., Menten K. M., Ott J., 2008, A&A, 485, 451
Holzmeier F., Lang M., Hader K., Hemberger P., Fischer I., 2013, J. Chem. Phys., 138, 214310
Huettemeister S., Wilson T. L., Bania T. M., Martin-Pintado J., 1993, A&A, 280, 255
Irvine W. M., Schloerb F. P., 1984, ApJ, 282, 516
Jiménez-Serra I. et al., 2016, ApJ, 830, L6
Jiménez-Serra I. et al., 2020, Astrobiology, 20, 1048
Jiménez-Serra I. et al., 2022, A&A, 663, A181
Jin M., Lee J.-E., Kim K.-T., 2015, ApJS, 219, 2
Koput J., 2003, J. Phys. Chem. A, 107, 4717
Krieger N. et al., 2017, ApJ, 850, 77
Lau K.-C., Li W.-K., Ng C. Y., Chiu S. W., 1999, J. Phys. Chem. A, 103, 3330
Lin M. C., He Y., Melius C. F., 1992, Int. J. Chem. Kinetics, 24, 1103
Liszt H., Lucas R., 2001, A&A, 370, 576
Liszt H. S., Lucas R., Pety J., 2006, A&A, 448, 253
Liszt H. S., Pety J., Lucas R., 2010, A&A, 518, A45
Loison J.-C., Wakelam V., Hickson K. M., 2014, MNRAS, 443, 398
Marcelino N., Cernicharo J., Roueff E., Gerin M., Mauersberger R., 2005, ApJ, 620, 308
Marston G., Nesbitt F. L., Stief L. J., 1989, J. Chem. Phys., 91, 3483
Martín S., Requena-Torres M. A., Martín-Pintado J., Mauersberger R., 2008, ApJ, 678, 245
Martín S., Martín-Pintado J., Blanco-Sánchez C., Rivilla V. M., Rodríguez-Franco A., Rico-Villas F., 2019, A&A, 631, A159
McElroy D., Walsh C., Markwick A. J., Cordiner M. A., Smith K., Millar T. J., 2013, A&A, 550, A36
McGuire B. A., 2022, ApJS, 259, 30
McKellar A., 1940, PASP, 52, 187
Muller S. et al., 2014, A&A, 566, A112
Muller S., Ubachs W., Menten K. M., Henkel C., Kanekar N., 2021, A&A, 652, A5
Nesbitt F. L., Marston G., Stief L. J., 1990, J. Phys. Chem., 94, 4946
Osamura Y., Petrie S., 2004, J. Phys. Chem. A, 108, 3615
Pazukhin A. G., Zinchenko I. I., Trofimova E. A., Henkel C., 2022, Astron. Rep., 66, 1302
Pineau des Forets G., Roueff E., Flower D. R., 1990, MNRAS, 244, 668
Requena-Torres M. A., Martín-Pintado J., Rodríguez-Franco A., Martín S., Rodríguez-Fernández N. J., de Vicente P., 2006, A&A, 455, 971
Requena-Torres M. A., Martín-Pintado J., Martín S., Morris M. R., 2008, ApJ, 672, 352
Rivilla V. M. et al., 2018, MNRAS, 475, L30
Rivilla V. M. et al., 2019, MNRAS, 483, L114
Rivilla V. M. et al., 2020, ApJ, 899, L28
Rivilla V. M. et al., 2021a, PNAS, 118, e2101314118

Rivilla V. M. et al., 2021b, MNRAS, 506, L79
Rivilla V. M. et al., 2022a, Frontiers Astron. Space Sci., 9, 829288
Rivilla V. M. et al., 2022b, Frontiers Astron. Space Sci., 9, 876870
Rivilla V. M. et al., 2022c, ApJ, 929, L11
Rodríguez-Almeida L. F. et al., 2021a, A&A, 654, L1
Rodríguez-Almeida L. F. et al., 2021b, ApJ, 912, L11
Sarrasin E., Abdallah D. B., Wernli M., Faure A., Cernicharo J., Lique F., 2010, MNRAS, 404, 518
Schilke P., Walmsley C. M., Pineau Des Forets G., Roueff E., Flower D. R., Guilloteau S., 1992, A&A, 256, 595
Swings P., Rosenfeld L., 1937, ApJ, 86, 483
Tafalla M., Myers P. C., Mardones D., Bachiller R., 2000, A&A, 359, 967
Talbi D., Ellinger Y., 1996, Chem. Phys. Lett., 263, 385
Tercero B., Cernicharo J., Cuadrado S., de Vicente P., Guélin M., 2020, A&A, 636, L7
Theule P., Borget F., Mispelaer F., Danger G., Duvernay F., Guillemin J. C., Chiavassa T., 2011, A&A, 534, A64
Turner B. E., Pirogov L., Minh Y. C., 1997, ApJ, 483, 235
Wakelam V. et al., 2012, ApJS, 199, 21
Wu Y. et al., 2019, A&A, 627, A162
Yamamoto S., Saito S., 1992, J. Chem. Phys., 96, 4157
Zeng S. et al., 2018, MNRAS, 478, 2962
Zeng S. et al., 2020, MNRAS, 497, 4896
Zeng S. et al., 2021, ApJ, 920, L27
Zhang W., Du B., Feng C., 2004, J. Mol. Struct.: THEOCHEM, 679, 121

APPENDIX A: SPECTROSCOPIC PARAMETERS OF H_2CN AND H_2NC EXCITED TRANSITIONS

Tables A1 and A2 list the H_2NC and H_2CN identified transitions towards G+0.693 cloud, respectively. We show only transitions with peak intensities of $T_A^* > 0.41$ mK, which correspond to $\sigma/3$ (where σ is the rms of the spectra), according to the LTE fit performed with MADCUBA. The last column (named 'Checked') indicates whether each particular transition has been used for the LTE fit (Yes) or not (No). All of the transitions listed in Tables A1 and A2 also appear in Fig. 1 (H_2NC) and Fig. 2 (H_2CN), respectively. Both tables provide the most relevant spectroscopic parameters for each transition, which are the rest frequency ν_{obs}, the quantum numbers of the levels involved in the transitions (N, K_a, K_c, J, F_1, and F), the energy of the upper level E_{up}, and their integrated intensity at 300 K (I). All of these transitions belong to ortho-H_2NC (Table A1) and ortho-H_2CN (Table A2), respectively. Spectroscopic information has been obtained from CDMS and Cabezas et al. (2021) for H_2NC, and from CDMS and Yamamoto & Saito (1992) for H_2CN.

Table A1. Main parameters of H_2NC transitions observed towards G+0.693 molecular cloud. The first column shows the rest frequency for each transition in units of GHz, while the next 12 gather the quantum numbers of the upper $(N', K_a', K_c', J', F_1', F')$ and lower $(N'', K_a'', K_c'', J'', F_1'', F'')$ levels, obtained from Cabezas et al. (2021) and CDMS. $\log I$ is the base 10 logarithm of the integrated intensity in units of nm^2 MHz at a fixed temperature of 300 K, and E_{up} is the energy in K of the upper level involved in the transition. The last column (named 'Checked') indicates whether each particular transition has been used to perform the AUTOFIT LTE fit (Yes) or not (No). All of the transitions belong to ortho-H_2NC.

ν_{rest} (GHz)	N'	K_a'	K_c'	J'	F_1'	F'	N''	K_a''	K_c''	J''	F_1''	F''	$\log I$ (nm^2 MHz)	E_{up} (K)	Checked
72.188 328	1	0	1	3/2	3/2	5/2	0	0	0	1/2	1/2	3/2	−4.497	3.5	Yes
72.189 077	1	0	1	3/2	1/2	3/2	0	0	0	1/2	1/2	1/2	−4.832	3.5	Yes
72.191 838	1	0	1	3/2	5/2	3/2	0	0	0	1/2	3/2	3/2	−5.068	3.5	Yes
72.194 219	1	0	1	3/2	5/2	7/2	0	0	0	1/2	3/2	5/2	−4.071	3.5	Yes
72.197 262	1	0	1	1/2	1/2	3/2	0	0	0	1/2	1/2	1/2	−4.974	3.5	Yes
72.198 211	1	0	1	3/2	3/2	1/2	0	0	0	1/2	3/2	3/2	−5.064	3.5	Yes
72.199 831	1	0	1	3/2	1/2	3/2	0	0	0	1/2	1/2	3/2	−4.872	3.5	Yes
72.202 571	1	0	1	3/2	5/2	3/2	0	0	0	1/2	3/2	1/2	−4.471	3.5	Yes
72.206 545	1	0	1	3/2	1/2	1/2	0	0	0	1/2	3/2	3/2	−4.901	3.5	Yes
72.208 502	1	0	1	3/2	3/2	5/2	0	0	0	1/2	3/2	5/2	−4.498	3.5	Yes
72.208 937	1	0	1	3/2	3/2	1/2	0	0	0	1/2	3/2	1/2	−4.902	3.5	Yes
72.209 450	1	0	1	3/2	3/2	3/2	0	0	0	1/2	3/2	3/2	−4.472	3.5	Yes
72.210 947	1	0	1	3/2	5/2	5/2	0	0	0	1/2	3/2	3/2	−4.199	3.5	Yes
72.212 383	1	0	1	1/2	3/2	5/2	0	0	0	1/2	1/2	3/2	−4.498	3.5	Yes
72.217 255	1	0	1	3/2	1/2	1/2	0	0	0	1/2	3/2	1/2	−5.066	3.5	Yes
72.217 855	1	0	1	1/2	3/2	3/2	0	0	0	1/2	1/2	1/2	−4.768	3.5	Yes
72.219 996	1	0	1	3/2	1/2	3/2	0	0	0	1/2	3/2	5/2	−4.846	3.5	Yes
72.220 178	1	0	1	3/2	3/2	3/2	0	0	0	1/2	3/2	1/2	−5.072	3.5	Yes
72.222 854	1	0	1	1/2	1/2	1/2	0	0	0	1/2	1/2	3/2	−4.705	3.5	Yes
72.225 310	1	0	1	1/2	3/2	1/2	0	0	0	1/2	1/2	1/2	−4.704	3.5	Yes
72.228 155	1	0	1	1/2	1/2	3/2	0	0	0	1/2	3/2	5/2	−4.557	3.5	Yes
72.228 583	1	0	1	1/2	3/2	3/2	0	0	0	1/2	1/2	3/2	−4.605	3.5	Yes
72.232 548	1	0	1	1/2	3/2	5/2	0	0	0	1/2	3/2	5/2	−4.501	3.5	Yes
144.361 610	2	0	2	5/2	5/2	7/2	1	0	1	3/2	3/2	5/2	−3.486	10.4	Yes
144.362 101	2	0	2	5/2	3/2	5/2	1	0	1	3/2	1/2	3/2	−3.698	10.4	Yes
144.362 392	2	0	2	5/2	7/2	9/2	1	0	1	3/2	5/2	7/2	−3.301	10.4	Yes
144.366 915	2	0	2	5/2	3/2	1/2	1	0	1	3/2	1/2	1/2	−4.305	10.4	Yes
144.369 440	2	0	2	5/2	7/2	5/2	1	0	1	3/2	5/2	3/2	−3.558	10.4	Yes
144.369 970	2	0	2	5/2	5/2	3/2	1	0	1	3/2	3/2	1/2	−3.919	10.4	Yes
144.373 607	2	0	2	5/2	3/2	5/2	1	0	1	3/2	3/2	5/2	−4.183	10.4	Yes
144.375 925	2	0	2	5/2	5/2	7/2	1	0	1	3/2	5/2	7/2	−4.163	10.4	Yes
144.376 393	2	0	2	5/2	5/2	3/2	1	0	1	3/2	5/2	3/2	−4.200	10.4	Yes
144.376 393	2	0	2	3/2	3/2	5/2	1	0	1	1/2	3/2	5/2	−4.326	10.4	Yes

Table A1 – *continued*

$\nu_{\rm rest}$ (GHz)	N'	$K'_{\rm a}$	$K'_{\rm c}$	J'	F'_1	F'	N''	$K''_{\rm a}$	$K''_{\rm c}$	J''	F''_1	F''	log I (nm^2 MHz)	$E_{\rm up}$ (K)	Checked
144.376 968	2	0	2	5/2	3/2	3/2	1	0	1	3/2	3/2	3/2	−4.183	10.4	Yes
144.377 018	2	0	2	5/2	5/2	5/2	1	0	1	3/2	5/2	5/2	−4.173	10.4	Yes
144.377 058	2	0	2	5/2	7/2	7/2	1	0	1	3/2	5/2	5/2	−3.401	10.4	Yes
144.377 058	2	0	2	3/2	5/2	7/2	1	0	1	1/2	3/2	5/2	−3.490	10.4	Yes
144.378 508	2	0	2	5/2	5/2	5/2	1	0	1	3/2	3/2	3/2	−3.645	10.4	Yes
144.379 862	2	0	2	5/2	3/2	3/2	1	0	1	3/2	1/2	1/2	−3.934	10.4	Yes
144.380 762	2	0	2	3/2	3/2	5/2	1	0	1	1/2	1/2	3/2	−3.907	10.4	Yes
144.383 214	2	0	2	3/2	3/2	3/2	1	0	1	1/2	1/2	1/2	−4.260	10.4	Yes
144.385 268	2	0	2	3/2	5/2	5/2	1	0	1	1/2	3/2	3/2	−3.664	10.4	Yes
144.390 759	2	0	2	3/2	1/2	3/2	1	0	1	3/2	1/2	3/2	−4.050	10.4	Yes
144.391 233	2	0	2	3/2	5/2	3/2	1	0	1	1/2	3/2	1/2	−3.854	10.4	Yes
144.391 233	2	0	2	3/2	1/2	1/2	1	0	1	1/2	1/2	3/2	−4.245	10.4	Yes
144.392 039	2	0	2	3/2	3/2	1/2	1	0	1	1/2	1/2	1/2	−4.136	10.4	Yes
144.398 146	2	0	2	3/2	3/2	3/2	1	0	1	1/2	1/2	3/2	−4.089	10.4	Yes
144.398 681	2	0	2	3/2	5/2	3/2	1	0	1	1/2	3/2	3/2	−4.274	10.4	Yes
144.400 428	2	0	2	3/2	3/2	5/2	1	0	1	3/2	3/2	5/2	−4.176	10.4	Yes
144.401 458	2	0	2	3/2	5/2	5/2	1	0	1	1/2	3/2	5/2	−4.139	10.4	Yes
144.415 423	2	0	2	3/2	5/2	7/2	1	0	1	3/2	5/2	7/2	−4.142	10.4	Yes

Note. Only transitions with intensities $T_{\rm A}^* > \sigma/3$ are considered and hence presented in this table.

Table A2. Same as Table A1, but for H_2CN. For this molecule, quantum numbers have been obtained from Yamamoto & Saito (1992) and CDMS. As in the case of H_2NC, all of the transitions belong to ortho-H_2CN.

$\nu_{\rm rest}$ (GHz)	N'	$K'_{\rm a}$	$K'_{\rm c}$	J'	F'_1	F'	N''	$K''_{\rm a}$	$K''_{\rm c}$	J''	F''_1	F''	log I (nm^2 MHz)	$E_{\rm up}$ (K)	Checked
73.324 939	1	0	1	3/2	3/2	5/2	0	0	0	1/2	3/2	5/2	−5.427	3.5	No
73.328 925	1	0	1	3/2	1/2	3/2	0	0	0	1/2	3/2	3/2	−5.412	3.5	No
73.342 507	1	0	1	3/2	1/2	3/2	0	0	0	1/2	1/2	1/2	−4.856	3.5	No
73.345 486	1	0	1	3/2	3/2	5/2	0	0	0	1/2	3/2	3/2	−4.636	3.5	No
73.349 203	1	0	1	3/2	1/2	1/2	0	0	0	1/2	1/2	3/2	−5.081	3.5	No
73.349 648	1	0	1	3/2	5/2	7/2	0	0	0	1/2	3/2	5/2	−4.446	3.5	No
73.355 762	1	0	1	3/2	7/2	3/2	0	0	0	1/2	3/2	1/2	−5.407	3.5	No
73.369 366	1	0	1	3/2	5/2	3/2	0	0	0	1/2	1/2	3/2	−4.863	3.5	Yes
73.392 507	1	0	1	3/2	3/2	1/2	0	0	0	1/2	3/2	1/2	−5.102	3.5	Yes
73.395 101	1	0	1	3/2	3/2	3/2	0	0	0	1/2	3/2	1/2	−4.872	3.5	Yes
73.408 673	1	0	1	3/2	3/2	3/2	0	0	0	1/2	1/2	3/2	−5.439	3.5	No
73.409 042	1	0	1	3/2	5/2	5/2	0	0	0	1/2	1/2	3/2	−4.588	3.5	No
73.444 240	1	0	1	1/2	3/2	5/2	0	0	0	1/2	3/2	5/2	−4.652	3.5	Yes
73.464 764	1	0	1	1/2	3/2	5/2	0	0	0	1/2	3/2	3/2	−5.445	3.5	No
73.465 480	1	0	1	1/2	3/2	3/2	0	0	0	1/2	3/2	3/2	−4.870	3.5	No
73.479 075	1	0	1	1/2	3/2	3/2	0	0	0	1/2	1/2	1/2	−5.423	3.5	No
73.485 656	1	0	1	1/2	3/2	1/2	0	0	0	1/2	1/2	1/2	−5.060	3.5	No
73.505 877	1	0	1	1/2	1/2	1/2	0	0	0	1/2	3/2	3/2	−5.061	3.6	No
73.510 462	1	0	1	1/2	1/2	3/2	0	0	0	1/2	3/2	5/2	−4.761	3.6	No
146.632 787	2	0	2	5/2	3/2	1/2	1	0	1	3/2	3/2	1/2	−5.590	10.6	No
146.640 124	2	0	2	5/2	5/2	3/2	1	0	1	3/2	5/2	5/2	−5.406	10.6	No
146.640 480	2	0	2	5/2	5/2	3/2	1	0	1	3/2	3/2	3/2	−5.499	10.6	No
146.643 059	2	0	2	5/2	5/2	3/2	1	0	1	3/2	3/2	1/2	−5.569	10.6	No
146.649 519	2	0	2	5/2	5/2	7/2	1	0	1	3/2	5/2	7/2	−4.933	10.6	No
146.656 268	2	0	2	5/2	3/2	5/2	1	0	1	3/2	3/2	5/2	−4.915	10.6	No
146.660 741	2	0	2	5/2	7/2	5/2	1	0	1	3/2	5/2	5/2	−4.605	10.6	No
146.661 097	2	0	2	5/2	7/2	5/2	1	0	1	3/2	3/2	3/2	−5.134	10.6	No
146.669 522	2	0	2	5/2	3/2	1/2	1	0	1	3/2	5/2	3/2	−5.257	10.6	No
146.672 825	2	0	2	5/2	3/2	5/2	1	0	1	3/2	1/2	3/2	−3.942	10.6	No
146.674 203	2	0	2	5/2	5/2	7/2	1	0	1	3/2	3/2	5/2	−3.804	10.6	No
146.675 065	2	0	2	5/2	7/2	9/2	1	0	1	3/2	5/2	7/2	−3.675	10.6	No
146.679 794	2	0	2	5/2	5/2	3/2	1	0	1	3/2	5/2	3/2	−4.424	10.6	No
146.689 681	2	0	2	5/2	3/2	1/2	1	0	1	3/2	1/2	1/2	−4.492	10.6	No
146.690 331	2	0	2	3/2	3/2	5/2	1	0	1	1/2	1/2	3/2	−5.206	10.6	No
146.699 950	2	0	2	5/2	5/2	3/2	1	0	1	3/2	1/2	1/2	−4.439	10.6	No

Table A2 – *continued*

ν_{rest} (GHz)	N'	K'_a	K'_c	J'	F'_1	F'	N''	K''_a	K''_c	J''	F''_1	F''	log I (nm^2 MHz)	E_{up} (K)	Checked
146.700 407	2	0	2	5/2	7/2	5/2	1	0	1	3/2	5/2	3/2	−4.030	10.6	No
146.706 337	2	0	2	5/2	3/2	3/2	1	0	1	3/2	3/2	3/2	−4.766	10.6	No
146.708 937	2	0	2	5/2	3/2	3/2	1	0	1	3/2	3/2	1/2	−4.203	10.6	No
146.712 990	2	0	2	5/2	5/2	5/2	1	0	1	3/2	5/2	5/2	−4.867	10.6	No
146.713 348	2	0	2	5/2	5/2	5/2	1	0	1	3/2	3/2	3/2	−3.972	10.6	No
146.721 851	2	0	2	5/2	7/2	7/2	1	0	1	3/2	5/2	5/2	−3.791	10.6	No
146.728 893	2	0	2	3/2	1/2	3/2	1	0	1	1/2	1/2	1/2	−4.848	10.6	No
146.744 745	2	0	2	3/2	5/2	5/2	1	0	1	1/2	1/2	3/2	−4.456	10.6	No
146.745 835	2	0	2	3/2	5/2	7/2	1	0	1	1/2	3/2	5/2	−3.929	10.6	No
146.748 675	2	0	2	3/2	5/2	3/2	1	0	1	1/2	1/2	3/2	−5.525	10.6	No
146.755 839	2	0	2	3/2	3/2	5/2	1	0	1	1/2	3/2	3/2	−4.088	10.6	No
146.756 570	2	0	2	3/2	3/2	5/2	1	0	1	1/2	3/2	5/2	−5.501	10.6	No
146.762 703	2	0	2	3/2	1/2	3/2	1	0	1	1/2	3/2	1/2	−4.389	10.6	No
146.769 300	2	0	2	3/2	1/2	3/2	1	0	1	1/2	3/2	3/2	−5.191	10.6	No
146.773 790	2	0	2	3/2	5/2	3/2	1	0	1	1/2	1/2	1/2	−4.724	10.6	No
146.785 361	2	0	2	3/2	3/2	3/2	1	0	1	1/2	1/2	3/2	−4.259	10.6	No
146.793 082	2	0	2	3/2	3/2	1/2	1	0	1	1/2	1/2	1/2	−4.471	10.6	No
146.807 617	2	0	2	3/2	5/2	3/2	1	0	1	1/2	3/2	1/2	−4.537	10.6	No
146.810 168	2	0	2	3/2	1/2	1/2	1	0	1	1/2	1/2	3/2	−4.392	10.6	No
146.810 268	2	0	2	3/2	5/2	5/2	1	0	1	1/2	3/2	3/2	−4.813	10.6	No
146.810 476	2	0	2	3/2	3/2	3/2	1	0	1	1/2	1/2	1/2	−5.545	10.6	No
146.810 984	2	0	2	3/2	5/2	5/2	1	0	1	1/2	3/2	5/2	−4.177	10.6	No
146.814 198	2	0	2	3/2	5/2	3/2	1	0	1	1/2	3/2	3/2	−4.544	10.6	No
146.833 500	2	0	2	3/2	3/2	1/2	1	0	1	1/2	3/2	3/2	−5.272	10.6	No
146.840 430	2	0	2	3/2	5/2	7/2	1	0	1	3/2	5/2	7/2	−4.363	10.6	No
146.851 599	2	0	2	3/2	3/2	3/2	1	0	1	1/2	3/2	5/2	−4.675	10.6	No
146.865 137	2	0	2	3/2	5/2	7/2	1	0	1	3/2	3/2	5/2	−5.550	10.6	No
146.875 854	2	0	2	3/2	3/2	5/2	1	0	1	3/2	3/2	5/2	−4.561	10.6	No
146.892 416	2	0	2	3/2	3/2	5/2	1	0	1	3/2	1/2	3/2	−5.519	10.6	No
146.905 561	2	0	2	3/2	5/2	5/2	1	0	1	3/2	5/2	7/2	−5.121	10.6	No
146.905 862	2	0	2	3/2	1/2	3/2	1	0	1	3/2	1/2	3/2	−4.738	10.6	No

Note. Only transitions with intensities $T_A^* > \sigma/3$ are considered and hence presented in this table.

APPENDIX B: H_2CN EXCITATION TEMPERATURE

Fig. B1 shows the best H_2CN LTE fit for six different T_{ex} ranging 3–8 K, focusing on the high-energy 2_{02}–1_{01} transitions. To obtain this fit, we have applied AUTOFIT using the four unblended 1_{01}–0_{00} transitions, while keeping fixed v_{LSR} and FWHM to the values derived for H_2NC (v_{LSR} = 71.0 km s^{-1} and FWHM = 18.3 km s^{-1}, see Section 3.1). It is clear that T_{ex} for H_2CN should be close to 3 K, since higher temperatures clearly overestimate the 2_{02}–1_{01} transitions, as indicated with green arrows in Fig. B1. Thus, we have assumed for the H_2CN fit the same T_{ex} as that found for H_2NC (3.28 K, see Sections 3.1 and 3.2).

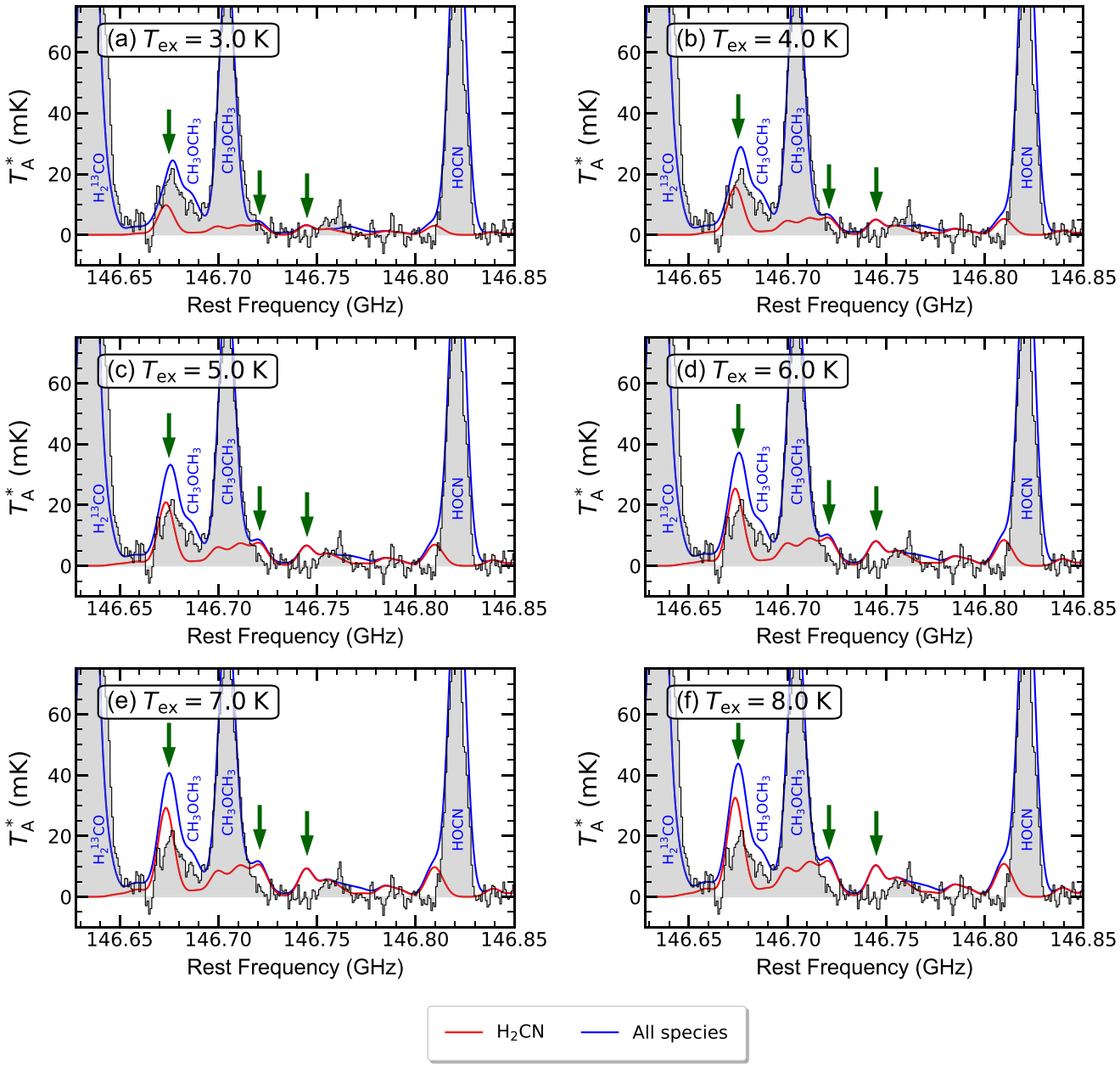

Figure B1. H_2CN LTE synthetic spectrum for the 2_{02}–1_{01} rotational transition in the range 146–147 GHz as a function of T_{ex}. Black histogram and grey shaded areas indicate the observed spectrum, while the red and blue lines indicate the emission of H_2CN and that of all the species already identified in the cloud (including H_2CN), respectively, whose names are indicated by the blue labels. Green arrows point to the H_2CN hyperfine transitions that have been used to constrain the T_{ex}.

This paper has been typeset from a TEX/LATEX file prepared by the author.